

## Article

# Cyclic Loading Test Conducted on the Bottom Joints of a Hybrid Precast Utility Tunnel Composed of Double-Skin Sidewalls and a Precast Bottom Slab

Weichen Xue \*, Shengyang Chen and Qinghua Wang

College of Civil Engineering, Tongji University, Shanghai 200092, China; chenshengyang@tongji.edu.cn (S.C.); wa\_zh@163.com (Q.W.)

\* Correspondence: xuewc@tongji.edu.cn; Tel.: +86-13701991855

**Abstract:** Four full-scale specimens were constructed, including two hybrid precast specimens with a haunch (height: 150 mm, PUT-H) and without a haunch (PUT). Additionally, two cast-in-place (CIP) comparative specimens (referred to as RUT-H and RUT) were included, all of which underwent reversed cyclic loading. The results showed that the four specimens suffered flexural damage at the ends of the sidewall and displayed similar hysteresis loops shapes. The bearing capacity of the PUT specimen was 2.7% higher than that of the RUT, while the bearing capacity of the PUT-H specimen was 8.5% lower than that of the RUT-H. Additionally, the displacement ductility values of the precast specimens PUT and PUT-H were 2.98 and 2.46, respectively, which are 11.3% and 3.53% lower than those of the corresponding CIP specimens. The haunch increases the local stiffness of the component, exerting a notable influence on the bearing capacity and displacement ductility of the specimens, increasing the bearing capacity by 20% and decreasing the ductility by 21%. Moreover, an assessment conducted using the criteria outlined in ACI 374.1-05 indicated that the four specimens exhibit excellent seismic performance.

**Keywords:** precast utility tunnel; cyclic loading; bearing capacity; displacement ductility; seismic performance



**Citation:** Xue, W.; Chen, S.; Wang, Q. Cyclic Loading Test Conducted on the Bottom Joints of a Hybrid Precast Utility Tunnel Composed of Double-Skin Sidewalls and a Precast Bottom Slab. *Buildings* **2024**, *14*, 341. <https://doi.org/10.3390/buildings14020341>

Academic Editor: Ehsan Noroozinejad Farsangi

Received: 31 December 2023

Revised: 19 January 2024

Accepted: 24 January 2024

Published: 26 January 2024



**Copyright:** © 2024 by the authors. Licensee MDPI, Basel, Switzerland. This article is an open access article distributed under the terms and conditions of the Creative Commons Attribution (CC BY) license (<https://creativecommons.org/licenses/by/4.0/>).

## 1. Introduction

A utility tunnel (UT) is a critical urban infrastructure that provides access to multiple utilities, including electrical power, telecommunications, gas, and water supply, and occasionally serves as an underground pedestrian pathway [1,2]. It is held in high regard by numerous countries for its benefits, including streamlined pipeline inspection and maintenance processes, minimized pipeline damage, and its role as a pivotal element in urban infrastructure, particularly in China [3,4].

Two primary approaches are employed for the fabrication of utility tunnels: cast-in-place (CIP) concrete and precast concrete methods [5,6]. Precast structures provide several benefits over CIP structures, including a standardized design, factory production for better quality control, mechanized installation, reduced energy consumption during construction, and improved rates of component recycling [7–9]. These advantages have found extensive applications in recent urbanization projects and have led to the development of three common prefabricated assembly schemes for UTs: integrated precast UTs, groove-shaped precast UTs, and hybrid precast UTs (HPUTs) [10]. The main feature of an integrated precast UT is its overall prefabrication in the cross-sectional direction. The central part of a groove-shaped precast UT is divided into two upper and lower groove-shaped precast blocks in the cross-sectional direction, which are connected at the construction site by prestressed ribs, bolts, etc. The construction of an HPUT involves the assembly of double-skin sidewalls and bottom and top slabs, all interconnected using CIP concrete. This construction approach

ensures excellent structural integrity and superior water resistance, making it a preferred choice in contemporary urban construction projects [11].

To model the shear deformation [12] of an HPUT, several pseudo-static tests were conducted. Yang et al. (2019) introduced an HPUT consisting of double-skin sidewalls, a double-skin bottom slab, and a laminated top slab. The influence of oil layer thickness and haunch height on mechanical behavior was examined via pseudo-static tests. The findings indicated that, within a certain range, augmenting the covering soil thickness increased the energy consumption capacity of the HPUT in later loading stages, and the specimens demonstrated significant structural deformability [13]. After that, we introduced another variant of the HPUT, which consists of three parts: double-skin sidewalls, a CIP bottom slab, and a laminated top slab. Anti-seismic tests were then conducted on full-scale joints and full-scale global specimens to explore the seismic performance of this type of UT. The experimental findings for both joint specimens and global specimens consistently demonstrated a bearing capacity, deformation capacity, and other hysteresis performance indicators equivalent to those of the CIP specimens [10,11].

Additionally, there are few structural design specifications for precast UTs. For instance, ACI 318-19 [14], the PCI Design Handbook (8th Edition) [15], Eurocode2 [16], NZS 3101 (2006) [17], and other specifications do not specify the design method and construction requirements of precast UTs. Japan's "Common Ditch Design Guidelines" (1991) [18] provide more detailed regulations and descriptions of the static and seismic design of CIP UTs but do not include sufficient information on the creation of a precast UT.

Based on the literature review presented herein, our main conclusions can be summarized as follows:

- (a) Hybrid precast utility tunnels possess excellent structural integrity and waterproofing performance, making them convenient for construction with relatively low technical requirements. This tunnel is a type of prefabricated concrete utility tunnel suitable for large-scale promotion.
- (b) Currently, the primary method of connecting the components of hybrid precast utility tunnels is through casting concrete in the core areas, which presents challenges in terms of on-site construction convenience.
- (c) The existing codes still fail to account for the seismic design provisions of hybrid precast UTs.

Considering the above, a new hybrid precast utility tunnel system created by transferring reserved rebars from the double-skin concrete sidewalls to the bottom slab is proposed herein. The aim is to increase on-site assembly efficiency and make said assembly more suitable for industrialized production by reducing on-site formwork installation, minimizing the risk of reinforcement collisions during component assembly, and streamlining various construction processes. To investigate the seismic behavior of the prefabricated UT mentioned above, low-cyclic-loading tests were conducted on the bottom joints, for which special emphasis was placed on analyzing the impact of the haunch on the mechanical properties of the specimens.

## 2. Experimental Section

### 2.1. Specimen

A precast utility tunnel composed of composite slabs located in China's middle-intensity (0.1 g) earthquake-resistant area was used as an engineering prototype. An assembly diagram of the precast specimen is shown in Figure 1.

A total of 4 full-scale model specimens of the bottom exterior joints of the UT were designed in this experiment, including a precast specimen, PUT; a precast specimen with a haunch (PUT-H), a CIP specimen, RUT; and a CIP specimen with a haunch (RUT-H). In specimen number, P stands for prefabrication, and R stands for CIP. The height, width, and longitudinal length of the four specimens are 2400 mm, 2000 mm, and 600 mm.

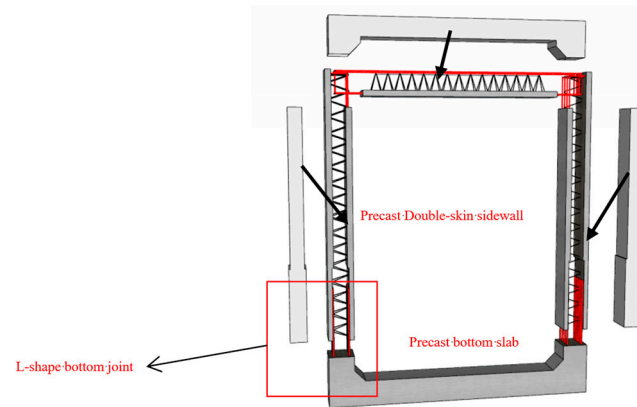


**Figure 1.** Assembly diagram of hybrid precast MU.

The thickness of both the sidewall and the bottom slab is 350 mm. The height of the haunch is 150 mm. The joint surface between the bottom slab and sidewall is positioned at a distance equal to one times the sidewall thickness (350 mm) above the bottom slab. Reinforcement proportions and component dimensions are shown in Figure 2. Specifically, the sidewalls of test pieces PUT and PUT-H are double-skin slabs with locally varying cross-sections on the outer blades, while the bottom slabs are CIP slabs. It is important to note that the lap length of the precast specimen's insert bars is 1.2 times the seismic anchorage length [19], and the truss bars of the precast specimen are arranged longitudinally in the middle.

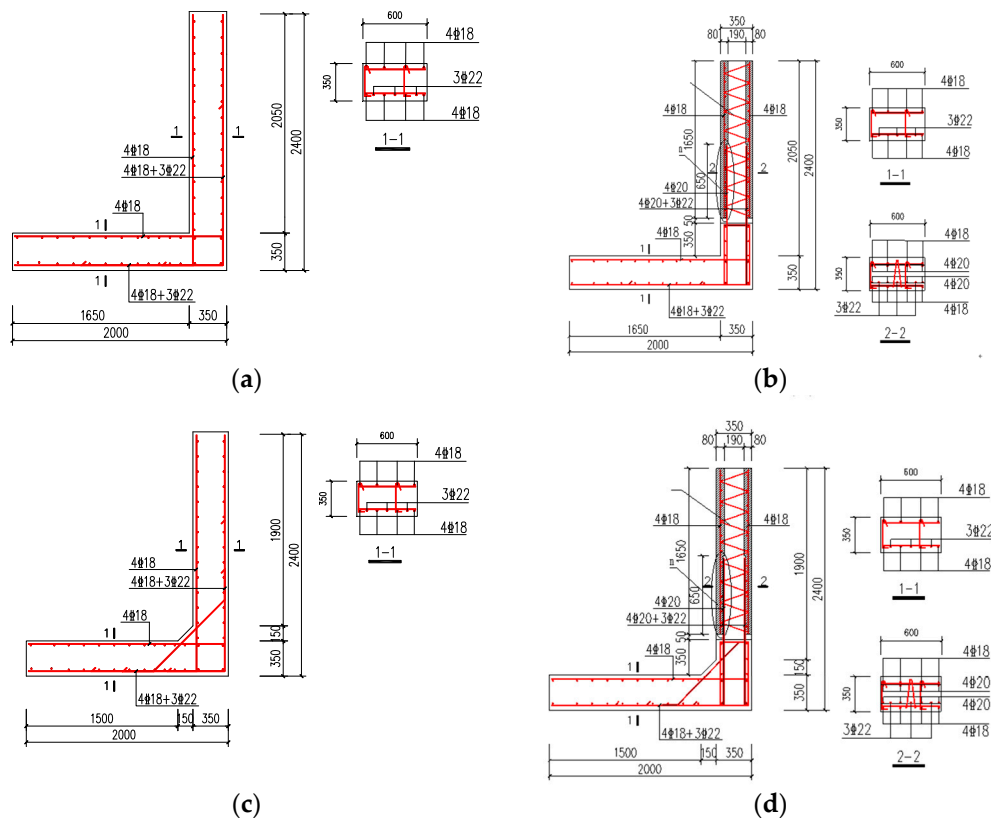


**Figure 2.** Reinforcement proportions and component dimensions of specimens. (a) RUT; (b) PUT; (c) RUT-H; (d) PUT-H.

## 2.2. Construction Method

The main production process of the test piece is as follows (Figure 3):

- (a) Bind the reinforcing bar cage of the double-skin sidewalls, insert the reinforcing bar into the mold, pour the outside slab of the sidewall, and reduce the concrete in the overlapping area of the additional reinforcing bar from 80 mm to 60 mm. Reserve space for the additional reinforcing bar, and then send it to the curing kiln for curing, as shown in Figure 3a.
- (b) When the strength of the concrete reaches the hoisting requirements, turn over the composite sidewalls and pour the inside slab of the sidewall, as shown in Figure 3b.
- (c) Hoist the composite sidewall, insert the additional reinforcement bars reserved for the CIP bottom slab into the cavity of the double-skin sidewall, and ensure that the inserted reinforcement adheres closely to the inner surface of the precast sidewall to limit the height of the section. When assembling, pay attention to leveling using a spirit level to ensure that the upper sidewall and the lower CIP bottom slab are aligned, as shown in Figure 3c.
- (d) After positioning, assembling, and fixing the composite sidewall and the CIP bottom slab, support the side formwork of the composite sidewall, use concrete to pour the middle mixed layer of the sidewall, and use vibrating rods for vibration and compaction, as shown in Figure 3d.



(a)



(b)



(c)



(d)

**Figure 3.** Test piece production. (a) Pouring the outside slab of the sidewall. (b) Pouring the inside slab of the sidewall. (c) Hoisting the composite sidewall. (d) Casting fresh concrete.

### 2.3. Material Properties

Four specimens were constructed using grade C40 concrete with a nominal cubic compressive strength of 40 MPa, and the reinforcements were fabricated with HRB400 steel bars (with a yielding strength of 400 MPa). The mechanical properties of concrete and steel reinforcements were tested in the Structural Laboratory of Tongji University according to GB/T 228.1-2010 [20]. The measured values are listed in Tables 1 and 2.

**Table 1.** Mechanical properties of concrete.

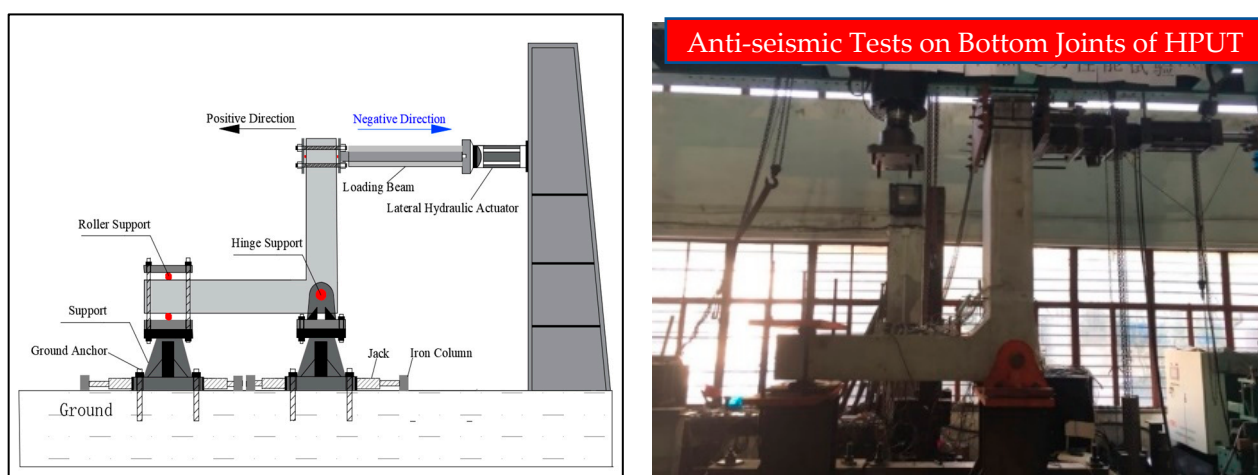
Specimen	Cube Strength $f_{cu}$ (MPa)	Prism Strength $f_c$ (MPa)	Elastic Modulus E (GPa)	Split Strength $f_t$ (MPa)
RUT and RUT-H	48.43	31.81	2.59	3.35
PUT and PUT-H	Precast part	49.30	2.61	3.41
	Post-cast part	53.29	2.72	3.47

**Table 2.** Mechanical properties of reinforcements.

Type	Diameter (mm)	Yield Strength $f_y$ (MPa)	Ultimate Strength $f_u$ (MPa)	Elastic Modulus E (GPa)	Elongation at Fracture (%)
HRB400	20	450.4	617.6	2.11	18.8
	18	423.5	556.7	2.01	18.5
	16	421.6	565.4	2.05	17.8
	14	437.1	580.7	2.13	17.0
	10	462.3	605.2	2.07	17.5
	8	487.2	610.7	2.06	17.8
	6	394.5	487.4	2.05	12.1

#### 2.4. Test Setup

This test was conducted in the laboratory of Tongji University using a 200 kN steel structure reaction frame. A 500 kN electro-hydraulic servo actuator was employed to apply horizontal repeated loads on the top of the wall. During seismic events, an underground utility tunnel is subjected to strain from the surrounding soil, leading to shear deformation. Therefore, for all four specimens, a loading method of applying horizontal reversed cyclic loading to the upper end of the sidewall was adopted to simulate the relative lateral displacement between the roof and floor of the utility tunnel during seismic activity, as depicted in Figure 4. One end of the bottom slab of the node was hinge-supported, while the other end was sliding-supported.

**Figure 4.** Experimental test setup.

The loading protocol was divided into two phases: (1) before cracking, wherein the specimen was load-controlled to determine the positive and negative cracking loads, and (2) after cracking, wherein the specimen was displacement-controlled, which consisted of three cycles of incremental reversed lateral displacement of  $\pm 1\Delta$ ,  $\pm 2\Delta$ ,  $\pm 3\Delta$ ,  $\pm 4\Delta$ ,  $\pm 5\Delta$ ,  $\pm 6\Delta$ ,  $\pm 7\Delta$ ,  $\pm 8\Delta$ , and  $\pm 9\Delta$ , as shown in Figure 5. In this study, the base displacement equaled 10.125 mm, as given by the equation  $0.005 H$ , where  $H$  is the height from the bottom support to the loading point (2025 mm).

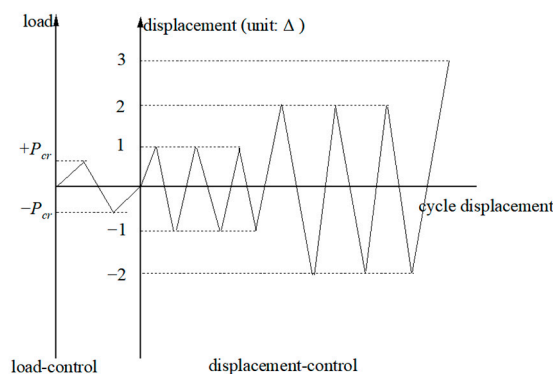


**Figure 5.** Loading history.

### 2.5. Instrumentation

The test process involved monitoring applied loads (measured by a load pressure sensor) and lateral displacements, sliding displacement, and the relative rotation angle (measured via LVDT). The steel bars requiring strain measurement were lightly polished, and strain gauges were adhered to the polished areas, which were protected with epoxy resin. At each level, phenomena were observed, and crack development was noted. Simultaneously, a combination of an automatic crack recognition instrument and a manually operated crack magnification device was used to measure crack width.

## 3. Result Analysis and Comparison

### 3.1. Overall Response and Failure Pattern

Figures 6 and 7 depict the failure modes of the components at different stages of the experiment. As illustrated in the figures, the following results were obtained:

- (1) Cracking stage. When the load reached the peak load of 0.37~0.57 times, the specimens cracked. The cracking loads of the PUT and RUT specimens without haunches were 30 kN and 25 kN, respectively, and the cracks were located on the lower surface of the sidewall joint and the junction between the lower end of the sidewall and the bottom slab, respectively. The cracking loads of the PUT-H and RUT-H specimens with haunches were 15 kN and 40 kN, respectively, and the cracks were located on the sidewall joint's lower surface and the sidewall's tip haunch, respectively. All the initial cracks were flexural cracks.
- (2) Yield stage. When the load reached 0.80~0.87 times the peak load, the steel bar began to yield gradually. The precast specimens PUT and PUT-H began to yield to tension (the steel bar strain was about  $2350 \mu\epsilon$ ), and the CIP specimens RUT and RUT-H were at the lower end of the sidewall near the tip of the haunch and the sidewall, respectively. The vertical steel bar at the junction of the lower end and the bottom slab began to yield to tension (the steel bar strain was about  $2300 \mu\epsilon$ ). With the increase in the load, the cracks of the PUT specimen were mainly concentrated in the joint sizing layer and the junction of the lower end of the sidewall and the bottom slab, all of which constituted horizontal bending cracks, and vertical bending cracks appeared at the junction of the bottom slab and the sidewall. The cracks of the RUT specimen were mainly distributed at the junction of the lower end of the sidewall and the bottom slab and gradually developed from the bottom to the top, and only a few vertical bending cracks appeared at the junction of the bottom slab and the sidewall. The cracks of PUT-H were mainly concentrated in the grouting layer of the joint, and only a few cracks appeared in other parts of the lower end of the sidewall, while no cracks were found in the bottom slab. The cracks of the RUT-H specimen were mainly distributed in the sidewall near the haunch variable cross-section area and gradually developed from the bottom to the top, and no cracks were found in the bottom slab.

- (3) Peak stage. Regarding the haunch-free specimens, PUT reached peak loads of 146.50 kN and 60.89 kN at forward and reverse displacement angles of 2.91% and 2.00%, while RUT reached peak loads of 148.35 kN and 60.89 kN at forward and reverse displacement angles of 3.52% and 1.99%. Regarding the specimens with haunches, PUT-H reached peak loads of 146.50 kN and 97.67 kN at forward and reverse displacement angles of 3.52% and 2.92%; RUT-H reached peak loads of 174.84 kN at forward and reverse displacement angles of 2.94% and 2.99%, and 90.11 kN was also reached. At this stage, the cracks in the specimen are basically uniform, and the horizontal bending cracks on both sides of the sidewall are symmetrically distributed; additionally, the cracks gradually widen and extend, and the concrete protective layer on both sides of the sidewall begins to be crushed and spalled. There were no obvious cracks between the outer blade of the sidewalls of the two precast specimens and the post-cast composite layer, indicating that the new and old concretes of the double-sided superimposed sidewalls of the precast specimens had good bonding performance.
- (4) Damage stage. After reaching the peak load, the specimen entered the failure stage. As shown in Figure 6, the final failure modes of the four specimens are all flexural failures. The failure positions of PUT and RUT were located at the end of the bottom slab, and the failure positions of PUT-H and RUT-H were located at the tip of the haunch at the end of the bottom slab. The type of flexion was exposed or compression flexion that bulged outward, and part of the longitudinal reinforcement was pulled off. Among the types of damage observed, the damage on the outer side of the lower end of the sidewall of RUT-H is also obvious. No obvious cracks were seen in the joint core area of all the specimens during the loading period, and the specimens remained intact until failure, meeting the design requirements of strong joints and weak members.

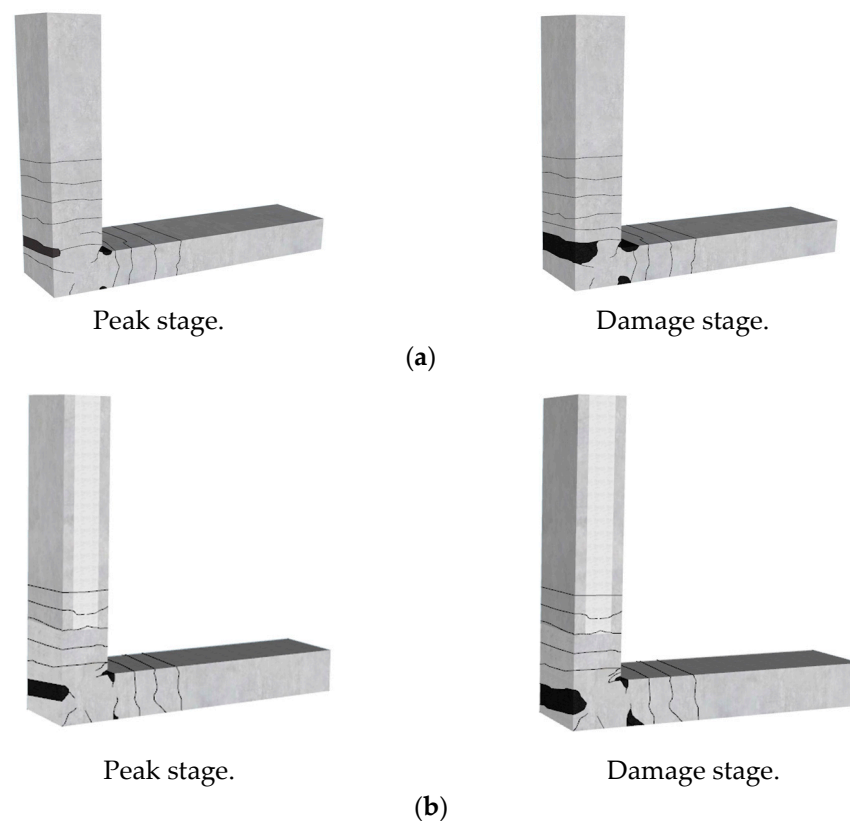
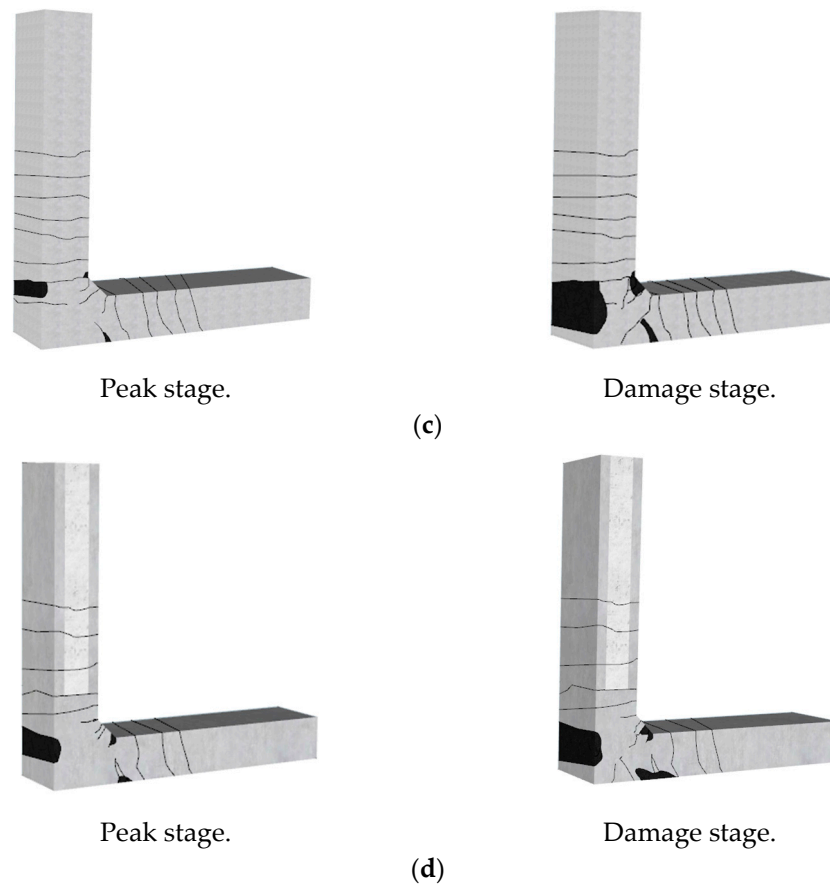
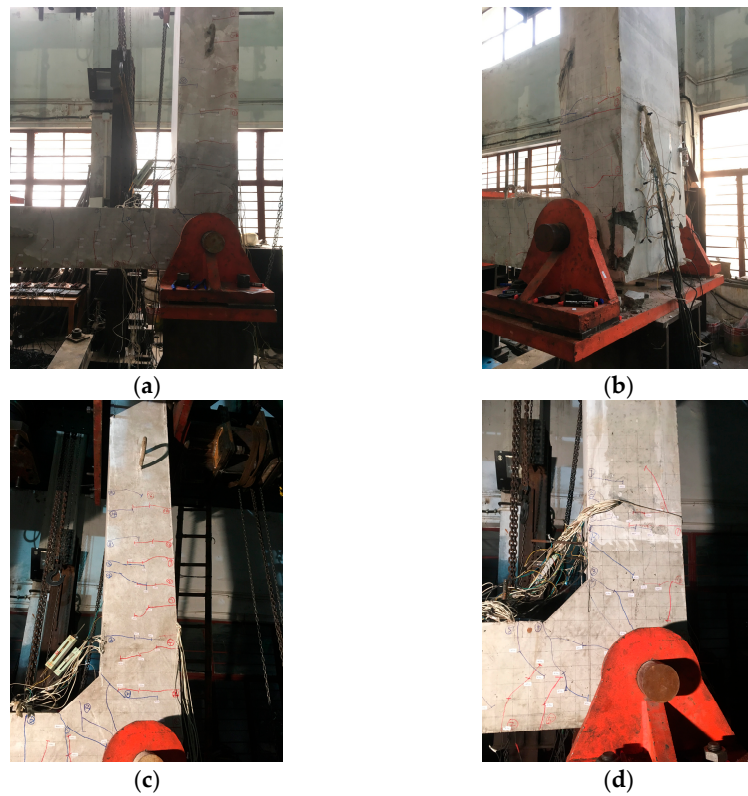


Figure 6. Cont.



**Figure 6.** Failure patterns of four specimens in peak and damage stages. (a). RUT. (b). PUT. (c). RUT-H. (d). PUT-H.



**Figure 7.** Photographs of specimens in the test. (a) RUT. (b) PUT. (c) RUT-H. (d) PUT-H.

### 3.2. Hysteresis Response

The hysteresis responses of the four specimens are presented in the load–displacement (drift ratio) curves shown in Figure 8, reflecting the seismic performance of utility tunnels, including the strength, deformation, and energy dissipation. The following can be gleaned from Figure 8:

- (1) Before the specimens crack, the horizontal load and displacement are approximately linear, and their structures are basically in the elastic stage, and their residual deformation and damage are slight. With the increase in displacement, the structures undergo plastic deformation, residual deformation increases gradually, and the enclosing area of the hysteresis curve also increases. In the later loading stage, the hysteresis curve appears to reflect a pinch effect due to the steel bar's yielding and the concrete's spalling.
- (2) At the same level of displacement, the load peak value of the first cycle is often higher than the latter two times, mainly due to the structure's damage accumulation and strength degradation. After the horizontal load reaches the peak value, the bearing capacity of the specimen decreases slowly with increasing horizontal displacement, showing good ductility.
- (3) The shapes and number of hysteresis loops of the CIP specimen and the precast specimen are similar, indicating that the energy dissipation performance and deformation capacity of the HPUT are similar to those of the comparative specimen. Throughout the loading process, the hysteresis loop shape transitioned gradually from a plum shape to an inverse S shape, and the energy dissipation capacity gradually decreased. This was mainly due to a large amount of spalling of the outer concrete and slippage between the outer longitudinal reinforcement and the concrete at the corner of the joint in the later loading stage.
- (4) Comparing the specimens with and without haunches, the shapes of the hysteresis loops are similar. The area enclosed by the hysteresis loop for the specimen with the haunch is more significant than that for the specimen without the haunch, and the energy dissipation performance is relatively good. The confinement of the concrete in the haunches reduced the damage to the sidewalls and slabs.

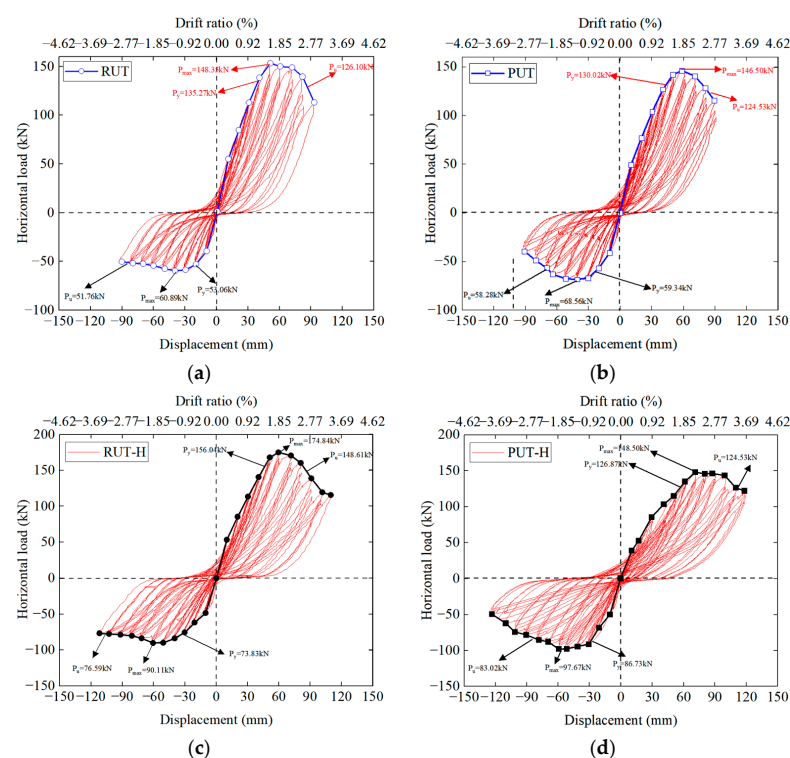
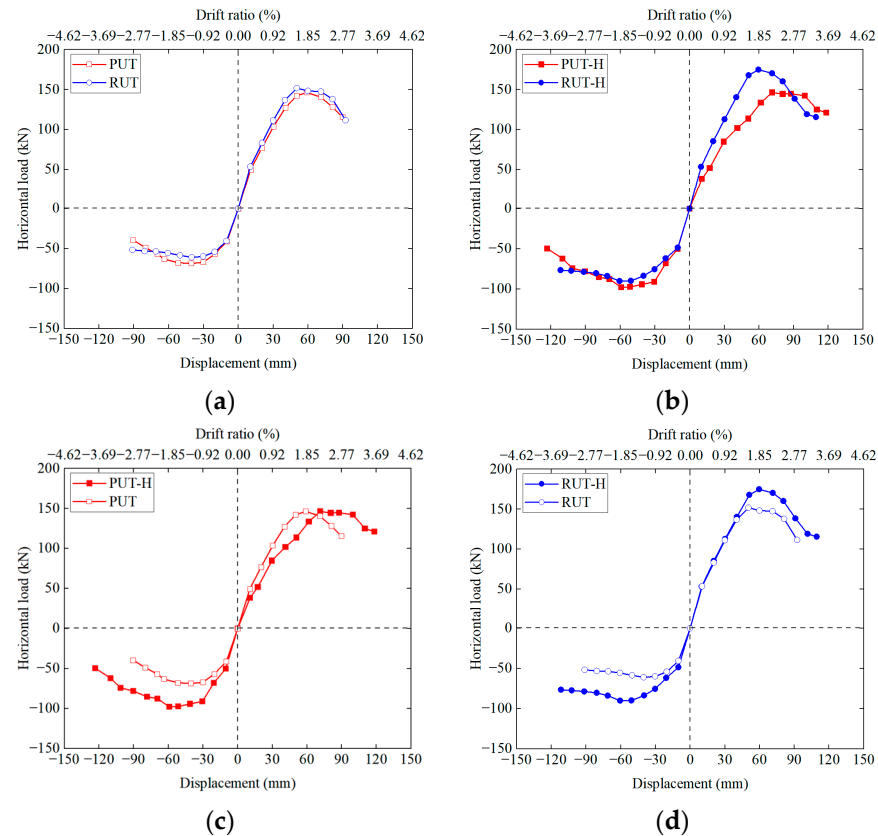


Figure 8. Hysteresis curves of four specimens. (a) RUT. (b) PUT. (c) RUT-H. (d) PUT-H.

### 3.3. Response Envelopes

The curve obtained by connecting the peak points of each loading in the same direction on a hysteresis curve is known as the skeleton curve, the outer envelope of the hysteresis curve. The skeleton curve can more clearly reflect a structure's strength, deformation, and other properties. The skeleton curves of the four specimens are shown in Figure 9.



**Figure 9.** Response envelopes. (a) PUT vs. RUT; (b) PUT-H vs. RUT-H; (c) PUT-H vs. PUT; (d) RUT-H vs. RUT.

As can be seen in Figure 9, the following results were obtained:

- (1) The skeleton curves of the four specimens have four characteristic points: cracking, yielding, reaching the peak value, and failure. The stress process of the structure can be divided into four stages: before cracking, when the load and displacement exhibit linear relationships; after cracking to before yielding, when the stiffness of the specimen decreases rapidly; after yielding to before reaching the peak point, when the skeleton curve becomes gentle; and after reaching the peak point, when the tangential stiffness of the specimen is negative, and its bearing capacity decreases slowly, showing good ductility.
- (2) The positive bearing capacity of each specimen was more significant than that in the negative direction. This can be attributed to the additional reinforcement installed at the corner on the positive side of the specimens, enhancing the positive load-bearing capacity of the joint. The positive bearing capacity of PUT is 1.35% lower than that of RUT, and the negative bearing capacity is 11.2% higher than that of PUT. The average bearing capacity of the PUT specimen is 2.7% higher than that of RUT. The positive bearing capacity of the precast specimen PUT-H is 16.2% lower than that of the CIP comparative specimen RUT-H, and the negative bearing capacity is 9.3% higher than that of the CIP comparative specimen. The average bearing capacity of the PUT-H specimen is 8.5% lower than that of RUT-H. It can be seen that the bearing capacities of the HPUT and the CIP specimen are similar.

- (3) The positive bearing capacity of the specimens PUT and RUT without haunches are 15.15%–1.35% lower than those with haunches (PUT-H and RUT-H). However, the negative bearing capacities of the specimens PUT and RUT without haunches are 29.80–32.4% lower than those with haunches. It can be seen that the reinforcement and concrete at the haunches have a stronger restraint effect when the exterior joints are subjected to a negative force.
- (4) The positive bearing capacity of the precast specimen PUT-H is 16.2% lower than that of the CIP comparative specimen. This difference may be attributed to the distinct failure sections of the precast and CIP specimens, with the CIP specimen failing at the upper part of the haunch, while the precast specimen failed at the lower part of the haunch.

### 3.4. Displacement Ductility and Deformability

Ductility reflects the deformation ability of a structure and is expressed by the ratio of the ultimate displacement to the yield displacement [21]. Yield displacement is determined using the energy method (Figure 10). The principle here is that the area  $A_{OF}$  is equal to the area  $ACD$  and that point E is determined [22]. The ultimate displacement is taken as the corresponding displacement value when the bearing capacity of the specimen drops to 85% of the peak load. The displacement ductility coefficients and load characteristic values of the four specimens are shown in Table 3. The following can be gleaned from Table 3:

- (1) The average ductility values of RUT, PUT, RUT-H, and PUT-H are 3.36, 2.98, 2.55, and 2.46, respectively. The ductility coefficients of both precast specimens are lower than this value for the CIP structure by  $-11.3\%$  and  $-3.53\%$ , respectively. The main reason for this could be the overlap of reinforcement in the core area of the precast elements, which, to some extent, increases the structural reinforcement ratio, enhances structural stiffness, and, consequently, affects the ductility coefficient of the structure.
- (2) The ductility of the precast specimen without a haunch is 11.3% lower than that of the CIP control specimen, while the ductility of the precast specimens with a haunch is 3.53% lower than that of the CIP comparative specimens. The main reason for this is that the haunch increases structural stiffness, thereby reducing the impact of the overlap zone reinforcement ratio of the precast element on the stiffness.
- (3) The impact of the haunch on the ductility coefficient is quite evident, causing a reduction of 17.40% in the ductility of the precast specimen and a reduction of 24.10% in the ductility of the CIP specimen.
- (4) The negative ductility of all the specimens is more pronounced than the positive ductility. This can be attributed to the significant peeling of material on the outer concrete at the corners of the joints during the later loading stages, resulting in bond slip between the external longitudinal reinforcement and the concrete, leading to a rapid decrease in bearing capacity.

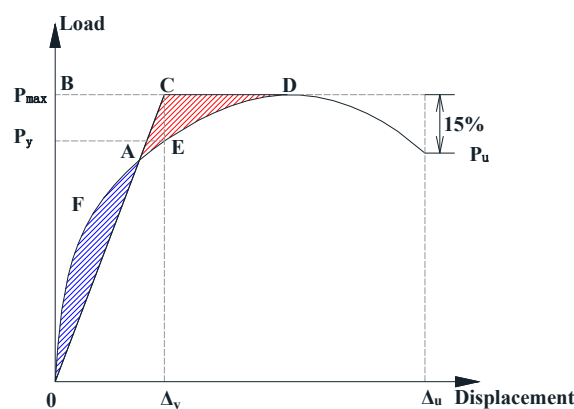


Figure 10. Method used to define yield and ultimate displacements.

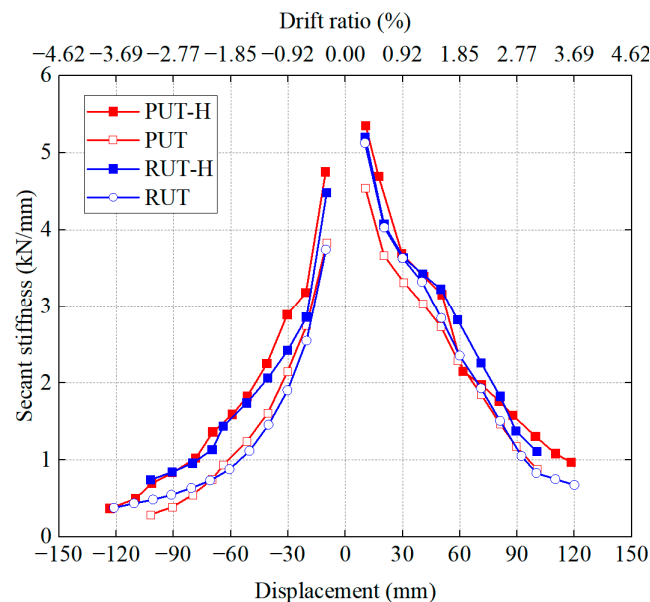
**Table 3.** Characteristic values and ductility of specimens.

Specimen		Crack Stage		Yield Stage		Peak Stage		Ultimate Stage		$\Delta_u/\Delta_y$	Ave
		$P_{cr}/kN$	$\Delta_{cr}/mm$	$P_y/kN$	$\Delta_y/mm$	$P_{max}/kN$	$\Delta_{max}/mm$	$P_u/kN$	$\Delta_u/mm$		
RUT	P	25.00	3.02	135.27	40.06	148.35	71.26	126.10	86.05	2.15	3.36
	N	15.00	1.80	53.06	19.53	60.89	40.26	51.76	84.36	4.31	
PUT	P	30.00	4.83	130.02	42.44	146.50	58.84	124.53	83.56	1.97	2.98
	N	25.00	3.25	59.34	19.65	68.56	40.50	58.28	76.08	3.87	
RUT-H	P	40.00	6.97	156.04	46.46	174.84	59.54	148.61	86.18	1.85	2.55
	N	40.00	5.90	73.83	32.72	90.11	60.46	76.59	106.51	3.26	
PUT-H	P	15.00	4.13	126.87	57.94	148.50	71.37	124.53	113.56	1.96	2.46
	N	30.00	4.22	86.73	28.64	97.67	59.18	83.02	84.65	2.96	

Note: P denotes positive direction. N denotes negative direction.

### 3.5. Deformability Stiffness Degradation

The secant stiffness degradation curves of the specimens are depicted in Figure 11.



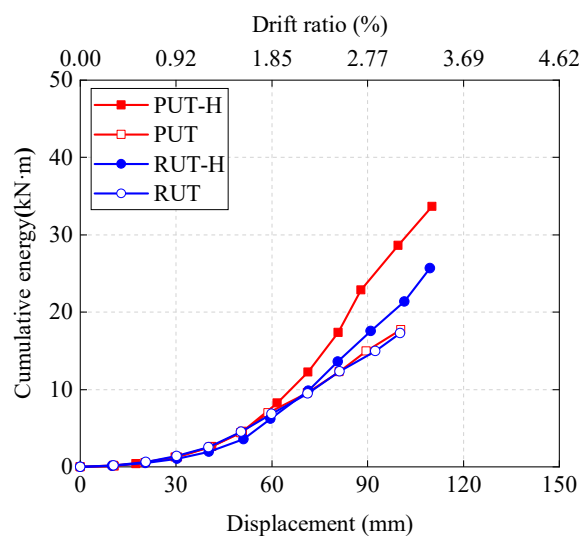
**Figure 11.** Stiffness degradation.

Figure 11 reveals the following:

- (1) The stiffness degradation laws of the four specimens are consistent, and the stiffness decreases rapidly in the early loading stage; with the increase in lateral movement, the decreasing stiffness trend slows. This indicates that the specimens' stiffness degradation is mainly concentrated in the early loading stage.
- (2) At all levels of displacement, the stiffnesses of the precast joint and the CIP comparison specimen are the same, indicating that the precast joint and the CIP comparison specimen show similar stiffness degradation characteristics.
- (3) In the early loading stage, the stiffness of the specimens with and without a haunch is basically the same; in the later loading stage, the specimen without a haunch degrades faster.

### 3.6. Energy Dissipation Capacity

The energy dissipation capacity is calculated from the area enclosed in the hysteretic loops by taking the average of three cycles at the same drift level. Thus, the cumulative energy dissipation is the accumulated sum of the energy consumed at each drift level. Figure 12. shows the cumulative energy dissipation of the two specimens.



**Figure 12.** Cumulative energy dissipation.

Figure 12 reveals the following:

- (1) When the load is small, the specimen is in the elastic stage and consumes less energy. With the increase in loading, the specimen enters the elastic-plastic stage, the steel bar gradually yields, concrete damage accumulates, and the energy dissipation capacity of each specimen increases continuously.
- (2) Compared with the CIP specimens, the energy dissipation capacities of PUT and RUT are comparable. The energy dissipation performance of PUT-H is higher than that of RUT-H. This indicates that the HPUT has an optimized local variable cross-section with an L-shaped reinforced connection, giving full play to its energy dissipation effect.
- (3) Regarding both the precast and CIP specimens, the energy dissipation capacity of the specimens with a haunch is higher than that of the corresponding specimen without a haunch. This shows that the haunch significantly influenced the energy consumption of the specimens. The main reason for this is that the load of the specimen with a haunch is higher than that of the specimen without a haunch under the same level of lateral movement. At the same time, the steel bars at the haunches yield, which contributes significantly to the energy consumption of the specimen.

#### 4. Seismic Performance Evaluation

The research shows that the underground structure analyzed herein is more vulnerable to earthquake damage [23]. During the 1995 Kobe Earthquake, transverse and longitudinal cracks and concrete spalling appeared in underground tunnels [24]. Therefore, the seismic performance of utility tunnels during subjection to strong earthquakes still requires proper evaluation methods. American code ACI 374.1-05 [25] provides a seismic performance evaluation method for frame structures under the effects of strong earthquakes. It is mainly implemented using quantitative indexes such as the bearing capacity, stiffness degradation, and energy dissipation capacity of specimens in the late loading period of the low-cycle load test. The mechanical behavior of underground utility tunnels in the direction of the cross-section is similar to that of frames. Furthermore, the internal force calculation model of a utility tunnel constitutes a closed frame model in the technical code for urban utility tunnel engineering (GB 50838-2015) [26]. Therefore, the hysteresis performance of the specimens could be evaluated in accordance with the guidelines of ACI 374.1-05.

The test results for comparison with the acceptance criteria in ACI 374.1-05 are listed in Table 4. The four specimens all satisfied the bearing capacity, stiffness degradation, and energy dissipation indexes, while the reverse bearing capacity index and forward and reverse stiffness degradation indexes of CIP RUT without a haunch were not satisfied, which is related to the appearance of a hysteresis loop in the later stage of loading. The

phenomenon of obvious pinching was consistent, and the main reason for its occurrence is that the protective layer of the lower end of the sidewall peeled off to a considerable degree; additionally, the reverse part of the steel bar peeled off. Compared with the haunch specimens, the evaluation index of the precast specimen PUT was significantly lower than that of PUT-H, and the evaluation index of the CIP specimen RUT was slightly lower than that of RUT-H. Therefore, the haunch had a more significant impact on the structure, a finding consistent with the analysis results in Section 3.

**Table 4.** Inspection of the tests in accordance with the acceptance criteria specified in ACI 374.1-05.

Indicator		RUT	PUT	RUT-H	PUT-H	Acceptance Criteria
$P_{lim}/P_{max}$	Positive	0.85	0.85	0.88	0.92	$\geq 0.75$
	Negative	0.84	0.75	0.89	0.89	
$K/K_{ini}$	Positive	0.21	0.12	0.18	0.29	$\geq 0.05$
	Negative	0.05	0.08	0.07	0.17	
Relative energy dissipation ratio $\beta$		0.21	0.14	0.14	0.23	$\geq 0.125$

Note:  $P_{lim}/P_{max}$ ,  $\beta$ , and  $K$  represent the load of the cycle at the drift ratio of 3.5% to the peak load, the area of the hysteresis loop at a drift ratio of 3.5% divided by the idealized elastoplastic energy, and the secant stiffness between  $-0.35\%$  and  $+0.35\%$  drift in the third cycle of a 3.5% drift, respectively.

## 5. Conclusions

Based on an experimental investigation of the bottom exterior joints of the HPUT composed of a double-skin sidewall and a precast bottom slab subjected to low cyclic loading, the failure pattern, bearing capacity, stiffness, ductility, and energy dissipation capacity of the specimens were analyzed and discussed. The following conclusions were drawn:

- (1) All the specimens suffered bending failure. The failure mode was as follows: the vertical steel bar at the lower end of the sidewall yielded to tension. The specific failure phenomenon was that the concrete on the outside of the wall or bottom slab spalled a lot, and the concrete on the inside was slightly crushed. The failure position of the four specimens was concentrated at the end of the sidewall or bottom slab.
- (2) The optimized reinforced connection with local variable cross-section can effectively transmit the steel stress. The difference between the load-bearing capacities of the precast specimen and the CIP comparison specimen was within 8.5%. The hysteresis curve shape, ductility, and stiffness degradation laws of the precast specimen are all close to those of the corresponding CIP specimens. In terms of energy consumption, the precast specimens had higher values than the CIP comparison specimens, and the specimens with haunches had significantly higher values than the corresponding specimens without haunches.
- (3) Haunches had obvious effects on bearing capacity, ductility, stiffness, and energy dissipation. They also had a significant impact on the bearing capacity and displacement ductility of the specimens, increasing the bearing capacity by 20% and decreasing the ductility by 21%.
- (4) A seismic performance evaluation was carried out according to ACI 374.1-05, and the precast specimens' bearing capacity, stiffness degradation, and energy dissipation indexes met the requirements, indicating that an HPUT composed of double-skin sidewalls and a precast bottom slab with reserved rebars exhibits excellent seismic performance.

**Author Contributions:** Conceptualization, W.X. and S.C.; methodology, W.X., Q.W. and S.C.; software, Q.W.; writing—original draft preparation, S.C.; writing—review and editing, W.X. and S.C.; funding acquisition, W.X. All authors have read and agreed to the published version of the manuscript.

**Funding:** This research was funded by the National Key Research and Development Program (Grant No. 2022YFB3706504).

**Data Availability Statement:** Data are contained within the article.

**Conflicts of Interest:** The authors declare no conflicts of interest.

## References

1. Luo, Y.; Alaghbandrad, A.; Genger, T.K.; Hammond, A. History and recent development of multi-purpose utility tunnels. *Tunn. Undergr. Space Technol.* **2020**, *103*, 103511. [[CrossRef](#)]
2. Gagnon, M.; Gaudreault, V.; Overton, D. *Age of Public Infrastructure: A Provincial Perspective*; Statistics Canada: Ottawa, ON, Canada, 2008; pp. 10–27.
3. Ministry of Housing and Urban-Rural Development of the People's Republic of China, 2022. 2021 Statistical Yearbook of Urban and Rural Development. Available online: <https://www.mohurd.gov.cn/gongkai/fdzdgnkr/sjfb/tjxx/jstjnj/index.html> (accessed on 1 September 2022).
4. Heilongjiang Daily, 2017. Construction of the Second Phase of the Underground Multiutility Tunnel Starts in Harbin City. People's Daily Online. Available online: <http://hlj.people.com.cn/n2/2017/0503/c220027-30124403.html> (accessed on 1 September 2022).
5. Yue, F.; Liu, B.; Zhu, B. Shaking table investigations on seismic performance of prefabricated corrugated steel utility tunnels. *Tunn. Undergr. Space Technol.* **2020**, *105*, 103579. [[CrossRef](#)]
6. De Sol, C. Guide Pratique des Galeries Multiréseaux. Techni. Cités. 2005. Available online: [https://www.academia.edu/36800248/Guide\\_pratique\\_des\\_galeries\\_multir%C3%A9seaux\\_par\\_le\\_groupe\\_de\\_recherche\\_CI%C3%A9\\_de\\_Sol](https://www.academia.edu/36800248/Guide_pratique_des_galeries_multir%C3%A9seaux_par_le_groupe_de_recherche_CI%C3%A9_de_Sol) (accessed on 1 April 2005).
7. Watanabe, E. Safety of bridges and breakwaters estimated through general principles for limit state design by Japan Society of Civil Engineers. *J. Theor. Appl. Mech.* **2012**, *50*, 871–883.
8. Liu, H.; Xu, C.; Du, X. Seismic response analysis of assembled monolithic subway station in the transverse direction. *Eng. Struct.* **2020**, *219*, 110970. [[CrossRef](#)]
9. Chen, J.; Xu, C.; El Naggar, H.M.; Du, X. Seismic response analysis of rectangular prefabricated subway station structure. *Tunn. Undergr. Space Technol.* **2023**, *131*, 104795. [[CrossRef](#)]
10. Xue, W.; Chen, S.; Song, Z. Pseudo-static tests on full-scale hybrid precast utility tunnel composed of double-skin sidewalls and cast-in-place bottom slab. *Structures* **2023**, *58*, 105573. [[CrossRef](#)]
11. Xue, W.; Chen, S.; Bai, H. Pseudo-Static Tests on Top Joints of Hybrid Precast Utility Tunnel. *Buildings* **2023**, *13*, 2567. [[CrossRef](#)]
12. Iwatate, T.; Kobayashi, Y.; Kusu, H.; Rin, K. Investigation and shaking table tests of subway structures of the Hyogoken-Nanbu earthquake. In Proceedings of the 12th World Conference on Earthquake Engineering, Auckland, New Zealand, 30 January–4 February 2000; New Zealand Society for Earthquake Engineering: Auckland, New Zealand; pp. 1043–1051.
13. Yang, Y.; Tian, X.; Liu, Q.; Zhi, J.; Wang, B. Anti-seismic behavior of composite precast utility tunnels based on pseudo-static tests. *Earthq. Struct.* **2019**, *17*, 233–244.
14. *ACI 318-19, 2019; Building Code Requirements for Structural Concrete and Commentary*. American Concrete Institute: Farmington Hills, MI, USA, 2019.
15. *PCI Design Handbook. Precast and Prestressed Concrete*, 8th ed.; Precast/Prestressed Concrete Institute: Chicago, IL, USA, 2017.
16. *EN-1992-1-1; Eurocode 2, Design of Concrete Structures—Part 1-1: General Rules and Rules for Buildings*. CEN European Committee for Standardization: Brussels, Belgium, 2004.
17. *NZS3101; The Design of Concrete Structures*. Standards Association of New Zealand: Wellington, New Zealand, 2006; p. 2006.
18. Japan Road Association. *Design Guidelines of Common Tunnel*; Tokyo Press, Japan: Tokyo, Japan, 1991.
19. Chen, G.; Chen, S.; Du, X.; Lu, D.; Qi, C. Review of seismic damage, model test, available design and analysis methods of urban underground structures: Retrospect and prospect. *J. Disaster Prev. Mitig. Eng.* **2016**, *36*, 1–23. (In Chinese)
20. *GB/T 228-2010; Metallic Materials-Tensile Testing Part 1: Method of Test at Room Temperature*. China Standards Press: Beijing, China, 2010.
21. Hu, X.; Xue, W.; Lv, Y. Seismic behavior of a new type of precast concrete shear wall using UHPC connections at boundary elements. *Eng. Struct.* **2024**, *302*, 117468. [[CrossRef](#)]
22. Park, R. Evaluation of ductility of structures and structural assemblages from laboratory testing. *Bull. N. Z. Soc. Earthq. Eng.* **1989**, *22*, 155–166. [[CrossRef](#)]
23. Hashash, Y.M.; Hook, J.J.; Schmidt, B.; John, I.; Yao, C. Seismic design and analysis of underground structures. *Tunn. Undergr. Space Technol.* **2001**, *16*, 247–293. [[CrossRef](#)]
24. Chen, J.; Jiang, L.; Li, J.; Shi, X. Numerical simulation of shaking table test on utility tunnel under non-uniform earthquake excitation. *Tunn. Undergr. Space Technol.* **2012**, *30*, 205–216. [[CrossRef](#)]
25. *ACI 374.1-05; Acceptance Criteria for Moment Frames Based on Structural Testing*. American Concrete Institute: Farmington Hills, MI, USA, 2005.
26. *GB 50838-2015; Technical Code for Urban Utility Tunnel Engineering*. China Planning Press: Beijing, China, 2015.

**Disclaimer/Publisher's Note:** The statements, opinions and data contained in all publications are solely those of the individual author(s) and contributor(s) and not of MDPI and/or the editor(s). MDPI and/or the editor(s) disclaim responsibility for any injury to people or property resulting from any ideas, methods, instructions or products referred to in the content.